2016

AN ASSESSMENT OF THE VALIDITY OF THE KINETIC MODEL FOR LIQUID-VAPOR PHASE CHANGE BY EXAMINING CRYOGENIC PROPELLANTS

Kishan Bellur
Michigan Technological University, ksbellur@mtu.edu

AN ASSESSMENT OF THE VALIDITY OF THE KINETIC MODEL FOR LIQUID-VAPOR PHASE CHANGE BY EXAMINING CRYOGENIC PROPELLANTS

By

Kishan Bellur

A REPORT

Submitted in partial fulfillment of the requirements for the degree of

MASTER OF SCIENCE

In Mechanical Engineering

MICHIGAN TECHNOLOGICAL UNIVERSITY

2016

This report has been approved in partial fulfillment of the requirements for the Degree of MASTER OF SCIENCE in Mechanical Engineering.

Department of Mechanical Engineering-Engineering Mechanics

Report Co-advisor: *Dr. Jeffrey Allen*

Report Co-advisor: *Dr. Chang Kyoung Choi*

Committee Member: *Dr. Gregory Odegard*

Committee Member: *Dr. Gowtham*

Department Chair: *Dr. William Predebon*

Contents

List of Figures

Abstract

Evaporation is ubiquitous in nature and occurs even in a microgravity space environment. Long term space missions require storage of cryogenic propellents and an accurate prediction of phase change rates. Kinetic theory has been used to model and predict evaporation rates for over a century but the reported values of accommodation coefficients are highly inconsistent and no accurate data is available for cryogens. The proposed study involves a combined experimental and computational approach to extract the accommodation coefficients. Neutron imaging is used as the visualization technique due to the difference in attenuation between the cryogen and the metallic container. Phase change tests are conducted using liquid hydrogen and methane at a range of saturation points between 15 psia and 30 psia. In order to account for the thermal gradient in the wall at the interface, a CFD thermal model is employed. Results from neutron imaging and the thermal model serve as boundary conditions to a transition film kinetic model. Using a combination of neutron imaging, CFD thermal model and kinetic model, there is a possibility to extract the accommodation coefficient while accounting for the curvature, disjoining pressure, nanoscale interactions and a variable wall temperature at the interface. An accommodation coefficient of 0.5705 ± 0.0001 is obtained for liquid hydrogen evaporating from a 10mm Al6061 cylinder at 21K using a constant wall temperature of 21.00005.

Chapter 1

Introduction

1.1 Motivation

Evaporation is ubiqitous in nature and occurs even in space. One of the key limitations to long term space missions is the ability to store and predict propellant behavior in a microgravity environment. Long term storage, transfer and predicting phase change of cryogenic propellants is mission critical technology [2]. Active and passive control technologies have been used to control propellant boiloff but phase change is inevitable. One passive fluid control method is the liquid acquisition device (LAD) that maintains a liquid film around the vapor [3]. The acquisition device is a screen that acts as a wicking structure to direct the flow of liquid. Several tests conducted at

NASA Glenn suggest that understanding of local thermodynamics at the interface is critical to predicting phase change. The experiments were focused on determination of bubble point pressure and vapor breakthrough for liquid hydrogen, oxygen and methane in LADs. It was noted that much of the uncertainty in the data could be attributed to evaporation at the screen surface [3, 4, 5]. The type of phase change encountered here is along the surface of the meniscus and is different from a pool boiling scenario where the pressure in the vapor and the wall temperature is sufficient to predict heat flux.

Computational Fluid Dynamics (CFD) modeling of the propellant along with a lumped parameter treatment of the vapor has been used to study pressurization in cryogen tanks and these have shown that a thin ($\approx$1mm) liquid layer separating the vapor phase from the wall is obtained [6, 7, 8, 9]. This type of modeling of propellant behavior utilizes the evaporation/condensation coefficients as inputs to capture phase change. This is particularly challenging due to the lack of reported evaporation/condensation coefficients and the ability to capture the local thermodynamics at the liquid vapor interface [10]. The evaporation/condensation coefficients, commonly clubbed together and referred to as the accommodation coefficient is a parameter introduced by kinetic theory as the ratio of the vapor molecules that get absorbed by the liquid surface to the number of vapor molecules incident on the liquid surface. This coefficient must be determined experimentally [11].

Additional factors affect meniscus phase change: curvature and the presence of a contact line. The curvature gives rise to a pressure jump across the liquid-vapor interface and the contact line results in a non-uniform evaporation over the surface [12]. The non-uniform evaporation over the surface is a result of the anisotropy of stresses in the thin liquid film due to disjoining pressure effects. Although curvature and disjoining pressure effects are incorporated into phase change models [13, 14], determining the correct accommodation coefficient remains a challenge and it is still unclear if the coefficient is a true thermodynamic property.

There are huge discrepancies in the reported values of accommodation coefficients. For water, the reported value of the accommodation coefficient spans three orders of magnitude depending on the method or the researcher conducting the experiment [15]. Initially reported by Cammenga et al. [16] and reiterated by Marek and Straub [15], a value of 0.002 was obtained as the evaporation coefficient for water in a glass vessel but when the same experiment was done with a similar copper vessel, the magnitude of the coefficient increased to values between 0.25 and 0.38. The only change was the wetting characteristics between the solid and liquid. The coefficient was determined from the bulk evaporation rate. Hence it is inferred that the wetting characteristics drastically affect evaporation and the reported values do not reflect the non-uniform evaporation due to the presence of a contact line. The objective of the proposed work is to shed light on why the coefficients measured in the past are inconsistent and to examine whether the coefficient is a true thermodynamic property. This is achieved

by analyzing the coefficients extracted for liquid hydrogen and liquid methane under various phase change conditions.

1.2 Kinetic Theory of Evaporation

Liquid vapor phase change is a complex, multi-scale problem and different phase change models have been used to quantify and predict mass transfer rates. These broadly fall under three categories: diffusive, kinetic or quantum mechanical. Diffusive models rely on partial vapor pressure as a trigger mechanism for evaporation. They predict the same phase change rates despite the solid wall material or the wetting characteristics and curvature of the liquid-vapor interface. The evaporative mass flux is only a function of the interfacial area and the concentration difference between the liquid and the interface (which is assumed to be a saturated vapor for modeling purposes). These models are typically applied to systems where surface area is huge, such as open reservoirs.

When the exposed surface area is smaller and comparable to the meniscus size, such as in porous structures or capillary tubes, kinetic models have been shown to be more accurate [17]. Kinetic theory based models can account for the effect of the wall, the location and size of the meniscus, curvature, interface temperature and disjoining pressure effects [18]. The classical kinetic theory has provided the basis for

understanding and modeling evaporation for over a century. Hertz [19] measured evaporation rates of mercury and from a theoretical analysis concluded that there exists a maximum rate of evaporation that depends on the temperature of the interface and the properties of the liquid. Knudsen [20] carried out similar experiments on evaporation of mercury and his results consistently indicated that the measured evaporation rate is lesser than the maximum rate suggested by kinetic theory. He introduced the concept of an evaporation coefficient to account for the deviation from the maximum evaporation rate.

The velocity distribution of the molecules is described by the Boltzmann equation (1.1).

$$\frac{\partial f}{\partial t} + c_i \frac{\partial f}{\partial x_i} = S(f) \tag{1.1}$$

where $S(f)$ denotes the collision term that describes the change of the velocity distribution due to intermolecular collisions and c_i is the velocity. In equilibrium, the velocity distribution function does not change with time and $S(f) = 0$. Hence the solution yields the famous Maxwellian distribution (1.2).

$$f_m = n \left(\frac{m}{2k\pi T} \right)^{\frac{3}{2}} \exp \left(-\frac{m}{2kT} (c_x^2 + c_y^2 + c_z^2) \right) \tag{1.2}$$

where k is the Boltzmann constant, n denotes the density number of particles, m is the molecular mass and T is temperature.

At a distance far away from the interface the velocity distribution is Maxwellian. If the interface itself is assumed to be a nondisturbing influence then the distribution would remain the same even in close proximity to the interface. In equilibrium, the rate of evaporation is equal to the rate of condensation. Assuming that the distribution is Maxwellian close to the interface, the Hertz-Knudsen equation for net phase change is the difference between rates of evaporation and condensation as shown by (1.3)

$$J = \frac{1}{\sqrt{2\pi mk}} \left(\sigma_e \frac{P_{sat}(T^L)}{\sqrt{T^L}} - \sigma_c \frac{P^V}{\sqrt{T^V}} \right) \tag{1.3}$$

where σ_e and σ_c are the evaporation and condensation coefficients, superscripts V and L denote the vapor and liquid phases respectively.

Schrage [21] assumed that the distribution in the vapor is better represented by a Maxwellian but with a net drift velocity (U_b) as shown in equation (1.4). He further states that the evaporation and condensation coefficients could be equal and clubbed together as one net coefficient.

$$f_s = n \left(\frac{m}{2k\pi T} \right)^{\frac{3}{2}} \exp \left(-\frac{m}{2kT} ((c_x - U_b)^2 + c_y^2 + c_z^2) \right) \tag{1.4}$$

Schrage proves that the effect of drift velocity is negligible if $U_b^2 << kT$. Using Schrage's modified distribution, equation (1.5) was obtained by Barrett and Clement

[22].

$$J = \frac{1}{\sqrt{2\pi mk}} \left(\frac{\sigma_e}{1 - 0.5\sigma_c} \frac{P_{sat}(T^L)}{\sqrt{T^L}} - \frac{\sigma_c}{1 - 0.5\sigma_c} \frac{P^V}{\sqrt{T^V}} \right) \tag{1.5}$$

Comparing (1.5) with (1.3) it is seen that when $\sigma_e = \sigma_c$, Schrage's equation predicts twice the mass flux as predicted by the Hertz-Knudsen expression. It is to be noted that all these analytical studies were performed for evaporation from a planar surface. If there exists a curvature and a contact line, the local pressure in the liquid film varies and significantly influences evaporation.

1.3 Evaporation at the contact line

The contact line is an apparent intersection of the three phases- solid, liquid and vapor. The contact angle is the apparent angle between the liquid and solid as measured through the liquid. The contact line is described as a continuum region that terminates in an adsorbed film. Figure 1.1 delineates the regions of interest in a wetting evaporating meniscus. The normal stress in the bulk is mostly influenced by capillary pressure or curvature. The adsorbed region comprises of a non-evaporating film where intermolecular forces dominate. This film is on the order of nanometers and is not optically accessible. The contact line region or the transition film region is influenced by both intermolecular forces and capillarity. It has been shown that for polar/non-wetting liquids, 60-90% of the evaporation occurs at the contact line

region [12]. The amount of mass transfer through the interface depends on the size of the contact line region as well as local thermodynamic properties.

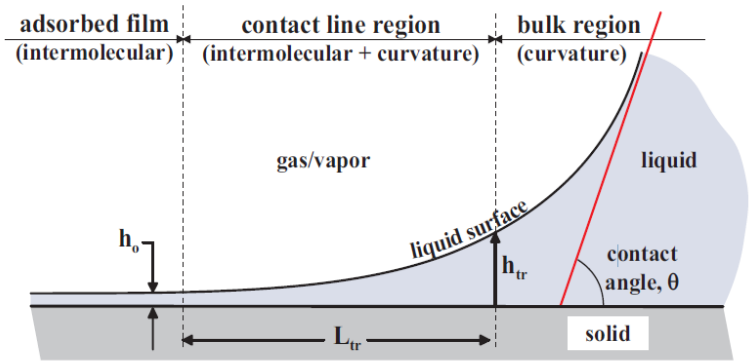

Figure 1.1: Regions of interest in an evaporating meniscus [1]

In order to solve for the evaporative mass flux using a kinetic model, the liquid phase temperature is required. The liquid temperature depends on the temperature of the solid in contact with the liquid. Meniscus phase change models typically use a constant superheat condition (a specified temperature offset between the saturated vapor and the solid wall) to model evaporation [23]. This value is difficult to estimate in the microscale region and it significantly influences the predicted evaporation flux. To obtain the actual wall temperature in the transition region, a conjugate heat transfer model that uses representative boundary conditions is used. A thermal CFD model is developed in ANSYS/FLUENT in order to obtain the temperature profile on the solid wall. Hence a variable wall temperature boundary can be implemented for accurate modeling and the need for a superheat condition parameter is obviated. The non-uniform evaporative flux in the contact line region is obtained from the kinetic

model using the results of the CFD model as thermal boundary conditions. The total evaporated mass can then be computed by integrating the non-uniform mass flux from the adsorbed film to the bulk meniscus.

Phase change experiments were conducted at the National Institute of Standards and Technology (NIST), Gaithersburg, MD, using neutron imaging as a visualization tool. Evaporation/condensation rates of hydrogenated propellants (liquid hydrogen, liquid methane) inside metallic containers of different materials and sizes are measured. The interface shape obtained from the results of the imaging experiments serve as physcial boundary conditions to the kinetic model while the CFD model provides the thermal boundary condition. Hence there is the possibility that the accommodation coefficients can be extracted by using a combination of the neutron imaging experiments, CFD thermal model and the kinetic transition film model. This is achieved by comparing the predicted evaporation rates to the experimentally measured evaporation rates with the accommodation coefficient as the only varying parameter.

Chapter 2

Neutron Imaging Experiments

Neutron imaging is a radiographic technique similar to x-rays, which makes use of the difference in attenuation characteristics of different elements [24]. Since neutrons have no charge, they do not interact with the electrons as x-rays do. However, they react strongly with the positively charged nucleus. Neutron imaging has been around for several decades now [25] but it was during the advances in digital cameras and image processing that it experienced a surge in interest as a reliable tool for non-destructive testing [26]. Despite having poor resolution, the ability to easily store and manipulate image data to make 3D tomography studies spurred the development of digital neutron imaging.

Neutron beams are broadly classified into three categories cold, thermal, and fast

depending on their energy. The mass attenuation coefficient of fast neutrons decreases with atomic number while that of x-rays increases [27] but no such correlation is found with respect to thermal neutrons [28]. Thermal neutrons are almost transparent to most metals but are strongly attenuated by materials such as hydrogen, boron, and cadmium. It is this difference in attenuation that allows for the visualization of the liquid hydrogen meniscus through an aluminum or stainless steel cylinder. Neutron imaging allows not only for qualitative measurements but also quantitative measurements of the geometry of the liquid hydrogen.

Cryogenic phase change experiments of liquid hydrogen were conducted during January 2015 and experiments with liquid methane were conducted in July and September 2015 at the NIST Center for Neutron Research in Gaithersburg, Maryland using their Neutron Imaging Facility (NIF). Thermal neutrons ($E \approx 25$meV) emitted from a fission reactor penetrate a 70 mm "orange" cryostat that cools the sample well containing either an Al6061 or SS316 test cell. The large neutron scattering cross section of hydrogen and methane in comparison to that of Aluminum and Steel allows for imaging the liquid hydrogen meniscus inside the test cells. A 20μm thick, 7.6 mg/cm^2 Gadoxysulfide screen is used as a scintillator while an Andor NEO sCMOS (scientific Complimentary Metal Oxide Semiconductor) camera with a pixel pitch of 6.5μm and variable exposure time is used to capture images. An 85mm Nikon lens with a PK-13 extension tube was used to focus the image on the scintillator.

The sample to be cooled by the cryostat is attached to the end of a long stainless steel stick and inserted into the central chamber of the cryostat. The cryostat consists of concentric jackets of cryogens and vacuum. The outer jacket is filled with liquid nitrogen that evaporates at atmospheric pressure maintaining a temperature of 77K. The inner jacket contains liquid helium that undergoes phase change and thereby cools the central sample well. The rate of helium phase change and as a result the temperature in the sample well is controlled by a throttling value referred to as the "cold" valve. For additional cooling, a vacuum can be pulled on the vapor side to increase phase change rate. The "cold" valve is in contact with a copper block that acts as a thermal contact between the evaporating helium and the sample well wall. The copper block is positioned at the separation of the cryostat and the lower chamber through which the neutrons pass. An electric heater is also placed in this block which acts as the heat source. The process of controlling temperature in the sample well is by adjusting the heating and cooling power by heater power in the copper block and the cold valve respectively. Heat is transferred to and from the sample well by a combination of conduction from the last Aluminum baffle down the stainless steel stick and into the test cell and by convection in the low pressure helium vapor in the sample well. Figure 2.1 shows the cryostat along with the stick and test cell.

A stainless steel lid is attached to the test cell using six Al 4-40 screws and an Indium O-ring. Four Si-diode (Lakeshore DT-640) temperature sensors are attached to the outer surface of the test cell using Al wire and SS springs. Additional details

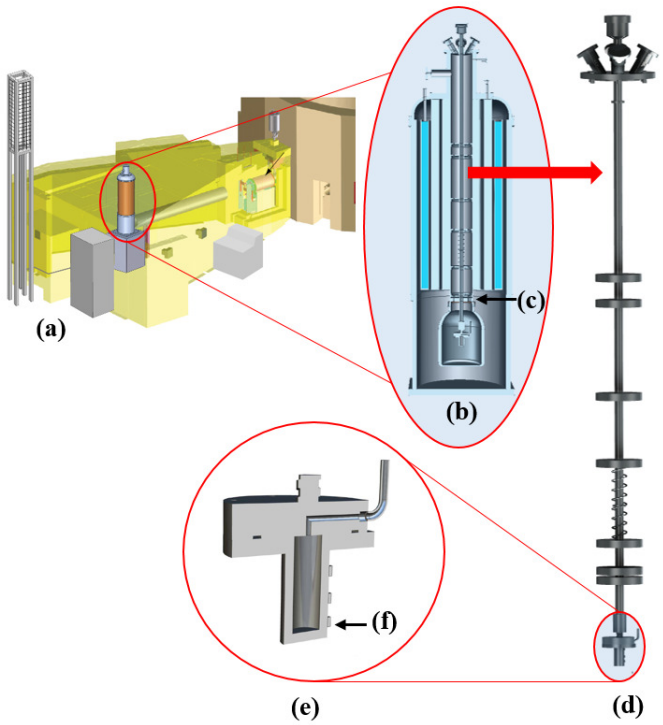

Figure 2.1: Experiment setup: (a) BT2 facility (b) 70 mm cryostat (c) Copper block assembly (d) Sample holder (e) Test cell (f) Si-diode sensor

on the experimental setup and procedure can be found in Bellur et al. [1]. Vapor (hydrogen/methane) at a set pressure is introduced into the test cell and the cryostat temperature is lowered below the saturation temperature to cause condensation. Consequently, to evaporate the liquid, the cryostat temperature is increased above the saturation temperature. Images are captured by the camera at an exposure of 10s. Using an edge detection algorithm, the meniscus shape and location is determined for each image. The volume of the liquid present in the test cell is then computed as a function of time. Figure 2.2 shows one such evaporation/condensation test. The contact angle for liquid hydrogen on Al6061 is determined to be $4\pm4^{\circ}$. The contact angle determination technique and image processing is detailed in Bellur et al [1].

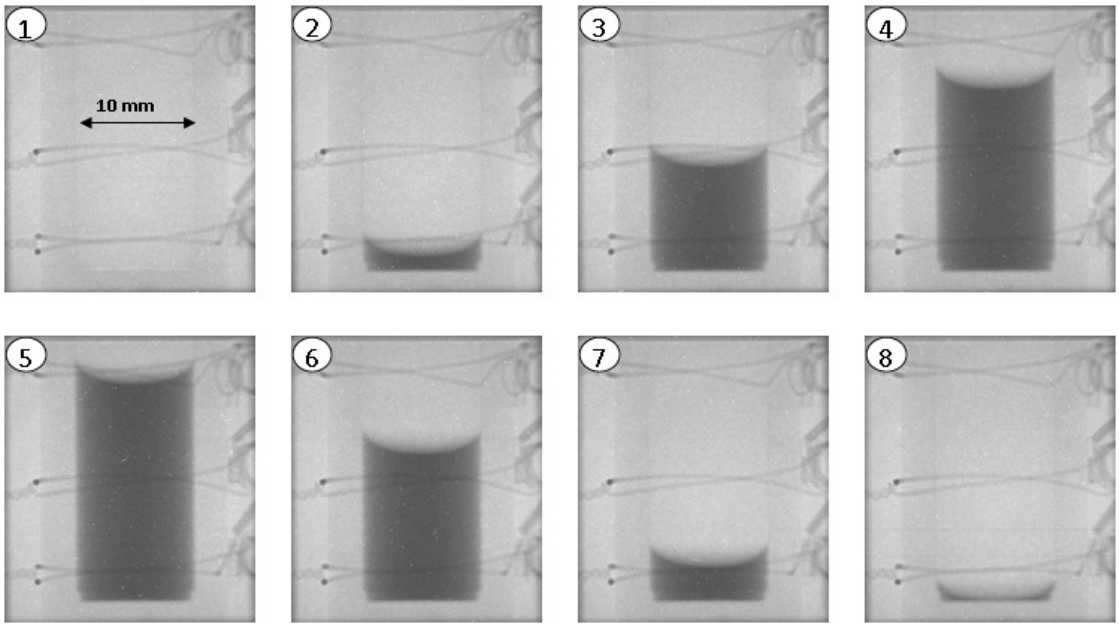

(a) Time lapse images of liquid hydrogen at a saturation of 21K

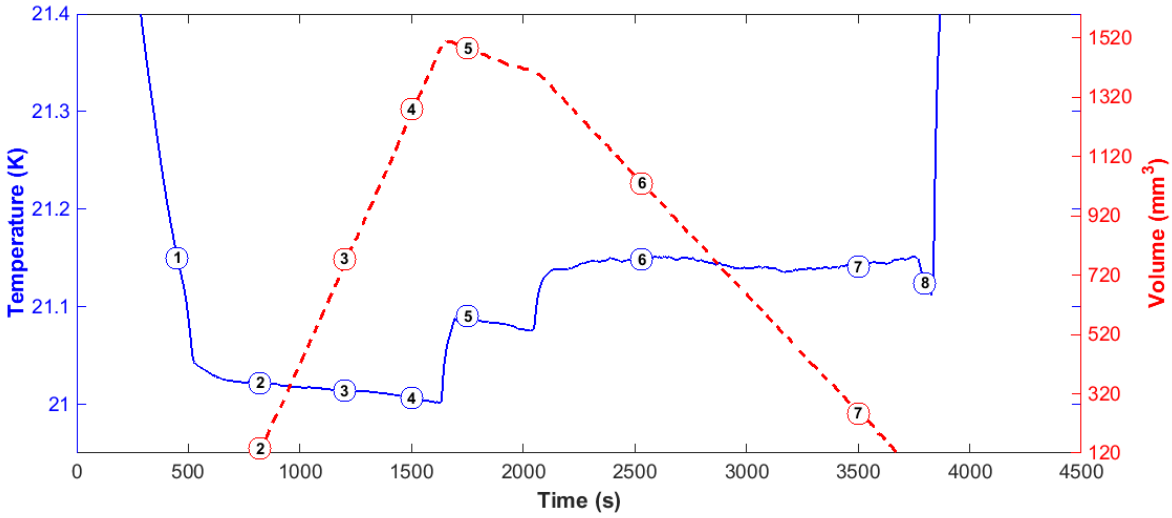

(b) Corresponding outer wall temperature and liquid volume

Figure 2.2: Neutron Imaging Cryo experiment results: Liquid hydrogen in a 10 mm Al 6061 cell

The Neutron Imaging experiments were done such that the pressure of the helium exchange gas in the sample well could not be measured. Even if this pressure could be

measured, the density of helium in the sample well would be difficult to determine due to the large temperature gradient ($\approx$ 20 K from the testcell up to the flange seal at $\approx$ 300 K). Further, no temperature measurements could be made on the inside of the test cells. In order to use the kinetic model to extract the accommodation coefficient, temperature distribution on the inside wall is a necessary boundary condition.

Chapter 3

Thermal Modeling

In order to obtain the appropriate thermal wall boundary condition, an axisymmetric computational thermal model is built in ANSYS/Fluent. Pressure-velocity coupling is implemented using the SIMPLEC (Semi Implicit Method for Pressure Linked Equations, Coupled) algorithm. Convergence criteria is set to 10^{-6} for all residuals of continuity, momentum and energy equations. The geometry of the thermal model comprises of the test cell, lid, sample stick, a radiation baffle and the copper block assembly as illustrated in Figure 2.1. Temperature dependent material properties from the NIST database are used for the simulation. Conduction down the stick and convection in the He vapor is then simulated by using the heater temperature from the experiments as a boundary condition. The experimental "dry" test is used to

"tune" the model so that the model's thermal transient results match the experimental results. Matching the model's results to temperature recorded by the four Si-diode sensors requires varying the thermal diffusivity of the helium and the contact resistance between the baffle and the copper block. The effective heat transfer conditions (thermal diffusivity and contact resistance) used to obtain the "matched" dry test response are then noted and used for subsequent phase change simulations. This procedure is repeated for each test cell. Figure 3.1 shows a "matched" dry test for the 10 mm Al 6061 cell.

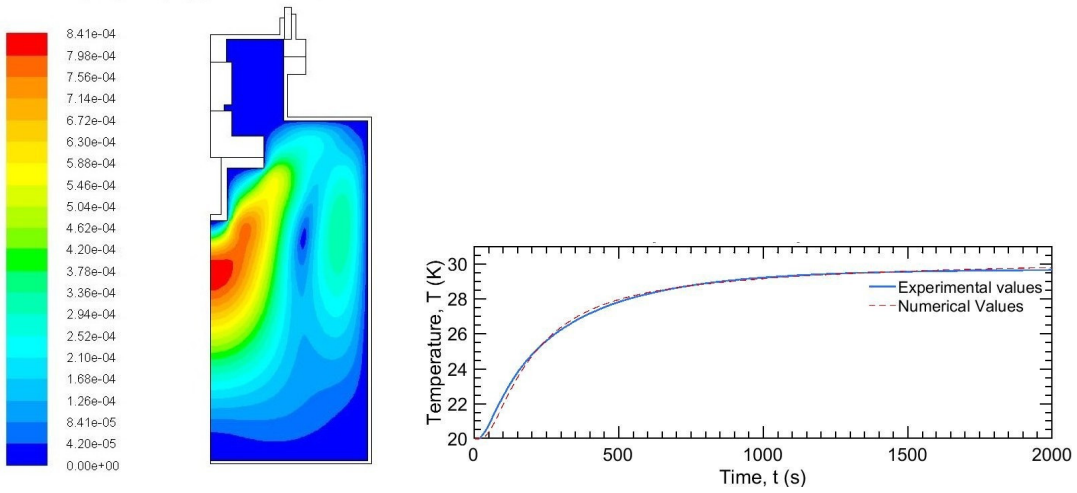

(a) Velocity contours at 2000s (b) Outer wall temperature: numerical vs experimental

Figure 3.1: A "matched" dry cell simulation for the 10mm Al6061 cell

Once the thermal response of the test cell is characterized, the liquid is inserted into the cell and modeled as solid block resembling the liquid shape and thermal properties. Modeling the liquid as a solid ensures that the level does not drop due to evaporation. Also, the simulation is faster as the need to solve for convection in

the liquid is obviated. A line sink is applied to model the evaporation from the liquid surface. Since most of the evaporation occurs near the wall, a line sink of length 10μm is applied on meniscus leading up to the solid wall. The flux applied on the line sink corresponds to the energy lost due to latent heat of vaporization at the evaporation rate measured experimentally. The inner wall temperature profile obtained will be used as thermal boundary conditions in the transition film model.

Chapter 4

Evaporation Modeling

4.1 Transition region kinetic model

It has been discussed that the curvature and contact line significantly influences evaporation and must be accounted for. The Hertz-Knudsen-Schrage equation although originally developed for a planar surface has been expanded to include surface tension effects [13] and curvature [14] effects using the Clayperon equation. The modified expression is given by equation (4.1) assuming $\sigma_e = \sigma_c = \alpha$.

$$J = \frac{2\alpha}{2-\alpha}\left(\frac{M}{2\pi R T_{lv}}\right)^{\frac{1}{2}}\left[\frac{p_v M h_{fg}}{R T_v T_{lv}}(T_{lv} - T_v) - \frac{V_l p_v}{R T_{lv}}(\Pi + \sigma\kappa) + \frac{M g p_v}{R T_v}x\right] \qquad (4.1)$$

where, J is the evaporative flux, α is the accommodation coefficient, T_{lv} is the interface temperature, Π is the disjoining pressure (a pressure reduction due to solid-liquid interaction in a thin film), σ is the surface tension, κ is the curvature while all other parameters represent standard thermodynamic properties.

The numerical model for the phase change in the transition region is built based on the formulation provided by Wee et al [23] and builds off of the code developed by Fritz [17]. Using a lubrication approximation, the film evolution/evaporation can be expressed as a nonlinear third order ODE such that all parameters and thermal properties are expressed in terms of the film thickness (4.2).

$$\begin{aligned} h_{xxx} - \frac{3h_{xx}^2 h_x}{1+h_x^2} - \frac{h_{xx}h_x}{(r_{ij}-h)^2} + \frac{h_x\left(1+h_x^2\right)}{(r_{ij}-h)^2} + \\ \frac{\gamma}{\sigma}\left(\frac{1+h_x^2}{r_{ij}-h} + h_{xx}\right)\frac{dT}{dx} + \frac{1}{\sigma}\left(1+h_x^2\right)^{\frac{1}{2}}\left(\frac{dp_l}{dx} + \frac{d\Pi}{dx}\right) = 0 \end{aligned} \tag{4.2}$$

where, h is the film thickness, r_{ij} is the radius of the cylinder, p_l is the pressure in the liquid, $\gamma = d\sigma/dt$, h_x, h_{xx} and h_{xxx} are the first, second and the third derivative of film thickness respectively.

The model is built using a one sided formulation approach. The liquid properties such as density, conductivity, etc are more dominant in the liquid than in the vapor. The model updates the liquid properties in each step of the simulation and assumes uniform properties in the vapor phase. Further, in the thin transition film, the bond number (gravitational forces/surface forces) is lesser than 1. Hence the effect of

gravity is neglected.

To keep the model in a steady state mode at each step of the simulation, the mass flux across the interface as determined by (4.1) is assumed to be replenished by liquid flow from the bulk meniscus. This conservation of mass at each step creates a pressure gradient along the simulated domain. The flow is modeled using a lubrication approximation of the Navier-Stokes equation in polar coordinates,

$$\frac{1}{r}\frac{\partial}{\partial r}\left(r\frac{\partial u}{\partial r}\right) = \frac{1}{\mu_l}\frac{dp_l}{dx} \tag{4.3}$$

where μ_l is the viscocity, u is the velocity, r is the local radius, dp_l/dx is the pressure gradient. The equation is solved by applying a no slip boundary condition at the wall and a free surface boundary condition at the interface(balancing viscous terms with surface tension terms).

$$\begin{aligned} &\text{at } r = r_{ij}, && u = 0 \\ &\text{at } r = r_{ij} - h, && -\mu\frac{\partial u}{\partial r} = \frac{d\sigma}{dx} \end{aligned}$$

Upon solving (4.3) using the given boundary conditions, an expression for $u(r)$ is obtained. The mass flux can then be expressed by (4.4)

$$J = \int_{r_{ij}-h}^{r_{ij}} \rho_l \left[u(r)\right] 2\pi r dr \tag{4.4}$$

Using the result of (4.1) and (4.4), dp_l/dx is evaluated for use in (4.2).

A simplified energy balance is expressed by (4.5)

$$k_l \frac{\partial}{\partial r}\left(r\frac{\partial T}{\partial r}\right) = 0 \tag{4.5}$$

A constant wall temperature boundary condition along with a heat flux boundary condition is used to solve the equation. The heat flux accounts for the conduction and the energy lost due to evaporation.

$$\begin{aligned} &\text{at } r = r_{ij}, && T = T_{wall} \\ &\text{at } r = r_{ij} - h, && k_l \frac{dT}{dr} = \dot{m}_{evap} h_{fg} \end{aligned}$$

Integrating (4.5) from wall to the interface (ie r_{ij} to $r_{ij} - h(x)$), the interfacial temperature is obtained (4.6)

$$T_{lv} = -\frac{h_{fg}}{k_l}\left(r_{ij} - h\right)\ln\left(\frac{r_{ij}}{r_{ij} - h}\right) + \dot{m}_{evap} + T_{wall} \tag{4.6}$$

Curvature gives rise to a pressure jump across the interface as described by the Young-Laplace equation. To effectively model the pressure balance, Wayner [14] proposed an augmented Young-Laplace equation (4.7).

$$p_v - p_l = \sigma\kappa + \Pi \tag{4.7}$$

The geometry of interest as seen in figure 1.1 has two planes of curvature, one due to the meniscus and the other due to the radius of the cylinder, in the azimuthal direction. Hence an effective 3D curvature is computed in equation (4.8).

$$\kappa = \left(\frac{1}{r-h}\right)\left(1+h_x^2\right)^{-1/2} + h_{xx}\left(1+h_x^2\right)^{-3/2} \tag{4.8}$$

For a flat wetting surface, the disjoining pressure is modeled by (4.9) considering only the intermolecular London-Van Der Waals forces[29]. More sophisticated models of disjoining pressure exist such as the logarithmic model by Holm and Goplen [30] or the contact angle based model by Wu and Wong [31]. For computation simplicity and due to the lack of data available for cryogens, the polynomial model given by equation (4.9) is used.

$$\Pi = \frac{A}{h^3} \tag{4.9}$$

where, A is a dispersion constant and 6πA is the Hamaker constant.

The evaporation in the model is accounted for by the Hertz-Knudsen-Schrage equation that has been expanded to include the effects of surface tension and curvature (equation (4.2)). The evaporation/condensation coefficients are inputs to the transition film evaporation model. The curvature is modeled using the augmented Young-Laplace equation by Wayner [14]. The film thickness of the non-evaporating adsorbed region (h) and the derivatives of film thickness (h_x and h_{xx}) are initial conditions to the model. The wall temperature profile is a necessary thermal boundary condition.

Although formulated as an initial value problem, the approach is to vary the initial conditions h_x and h_{xx} such that the curvature from the simulation can be matched to the interface curvature acquired from Neutron Imaging. The ODE is numerically solved using a 2^{nd} order Runge-Kutta method using a simple backward Euler finite difference scheme for local interface temperatures and surface tension gradients. At each step in the simulation, the evaporated mass flux and interfacial temperature is computed and the corresponding parameters are updated.

Using the Young-Laplace curve fits from the neutron images as physical boundary conditions, a shooting method is employed for the transition film model. The initial conditions at the adsorbed film are varied such that the slope and curvature obtained from the model at its end boundary condition matches the bulk meniscus represented by the Young-Laplace curve fit within a 1% error. Assuming no evaporation in the adsorbed film region, the non-uniform evaporative flux obtained in the transition region is then integrated along the liquid interface to obtain the total evaporation rate. The temperature gradient at the wall obtained from the CFD model serves as the thermal wall boundary condition.

The code is built using a modular approach comprising of various submodels to account for curvature, disjoining pressure and other parameters. The model contains a library of fluids (currently- water, pentane, octane, hydrogen and methane) with the parameters built in and different geometries can be implemented if necessary. The

code is built such that switching between different fluids or geometries is straightforward. This enables adaptability of the code to model both hydrogen and methane evaporation in cylinders of different geometries and cell materials.

The transition film evaporation model is currently built assuming the Maxwellian distribution and does not account for the collisional effects described by the Boltzmann equation.

4.2 Velocity distribution near the interface

The Schrage formulation makes a half sided Maxwellian assumption which is the result of including a drift velocity in the vapor phase distribution as seen in equation (1.4). Molecular Dynamics (MD) simulations have shown that the distribution of molecules in the vapor phase deviates from the Maxwellian distributions at low temperatures [32]. Further, it is seen from equation 1.1 that in a non-equilibrium situation the collision term cannot be neglected. Non-equilibrium solutions of the Boltzmann equation are complex involving either direct computation or Monte Carlo simulations [33]. A widely used approximation is one that replaces the collision term with a simpler expression. Bhatnagar et al [34] and Welander [35] propose a simple collision term called the BGKW model. Ytrehus [36] compared the BGKW equation and Monte Carlo simulations to both the Hertz-Knudsen formulation and the Schrage

equation and found that the Hertz-Knudsen equation underestimates the mass flux by an factor of 2 and the Schrage equation slightly overestimates the mass flux. It is argued that this is due to the fact that the Schrage equation ignores the effects at the Knudsen layer. Labuntsov [37] revised the Schrage expression to consider Knudsen layer effects but Barret and Clement [22] suggest that the distribution may violate the conservation of energy and momentum.

An alternative is the Chapman-Enskong (CE) method that involves expanding the distribution function about the Knudsen number. The first order CE expansion of the Boltzmann equation, ignoring the shear stresses gives the distibution described by equation 4.10 [33].

$$f_{CE} = f_M \left(1 - \frac{2}{5}\frac{\kappa}{Rp} C_k \left(\frac{C^2}{2RT^2} - \frac{5}{2T}\right)\frac{\partial T}{\partial x_k}\right) \tag{4.10}$$

Where, f_M is the equilibrium Maxwellian distribution.

It is seen that there is a need to carefully account for the collisional changes that occur in the Knudsen layer. Molecular dynamics (MD) simulations are ideal for extracting velocity distibutions. In order to obtain a modified Maxwellian distribution at the interface a Molecular Dynamics study will be conducted using the LAMMPS code.

A non-equilibrium MD simulation using a Leonard Jones potential fluid and parallel solid walls at different temperatures is proposed. The two walls are held at different

temperatures with hydrogen/methane between them at an average temperature. It has been shown that this condition leads to condensation on the cooler wall and evaporation at the hotter wall [38, 39]. The results of the simulation are then used to extract the modified Maxwellian distribution in the Knudsen layer of the interface. This distribution can then be used to develop a modified expression for evaporative flux that incorporates curvature, disjoining pressure and the Knudsen layer effects.

4.3 Thickness of non-evaporating adsorbed film

The film thickness in the non-evaporating adsorbed film region is a necessary initial condition for the model. It is evaluated by setting (4.1) to zero and determining the film thickness. However, it was noted that the computed value is extremely sensitive to T_{lv} and in the case of hydrogen changes from <1nm when $T_{lv} = T_{wall}$ to 240nm when $T_{lv} = T_v$ (the saturation condition), even though the $T_{wall} - T_v < 0.1$K. The selected value of temperature and adsorbed film thickness significantly affects the film profile and computed evaporation flux thereby varying the accommodation coefficient obtained. Typically this film is only a few nanometers thick and is not optically accessible as it is smaller than the wavelength of visible light. The CFD thermal model does not have the resolution or the capability to capture the physics of this ultra thin film. Hence a more sophisticated method is necessary to fix this initial condition.

Non-evaporating adsorbed film has been succesfully simulated using MD [38, 39]. These simulations were performed for Argon on a Platinum surface and showed that a non-evaporating adsorbed film is formed. The objective of these studies were not to study the film thickness but to study evaporation. However, they have shown that if the simulations are run for a sufficiently long time, most of the liquid evaporates leaving behind an adsorbed film that is only a couple of nanometers thick. The non-evaporating film was found to be 1.3nm in the case of Argon on Platinum [38]. Hence the thickness of this adsorbed film can be measured by MD simulations with reasonable accuracy. The measured thickness can directly be used as an initial condition in the model and a corresponding T_{lv} can be computed by setting (4.1) to zero. It has further been shown that the Hamaker constant can be extracted from MD simulations of a non evaporating adsorbed film [40].

Chapter 5

Extraction of accommodation coefficients

The accommodation coefficient being an input to the transition film model, is varied till the total evaporation flux obtained from the model matches that obtained from the neutron imaging experiments. Figure 5.1 shows one such simulation where the results from the transition film model have been matched to the data obtained from the neutron images for a constant temperature wall boundary condition. The wall temperature in the adsorbed film region is assumed to be equal to the saturation temperature while a wall superheat is imposed in the transition film region. This causes a discontinuity in evaporation flux at $x = 0$. This is further evidence that the model is very sensitive to the initial conditions specified. The accommodation

coefficient for constant wall superheat of 50 μK using saturated hydrogen at 21K and a contact angle of 0° with Al6061 is found to be 0.5705 ± 0.0001.

The model, however, is formulated to have a variable wall temperature boundary and the temperature profile obtained from the CFD thermal model will be implemented in lieu of the constant temperature wall for a more accurate accommodation coefficient.

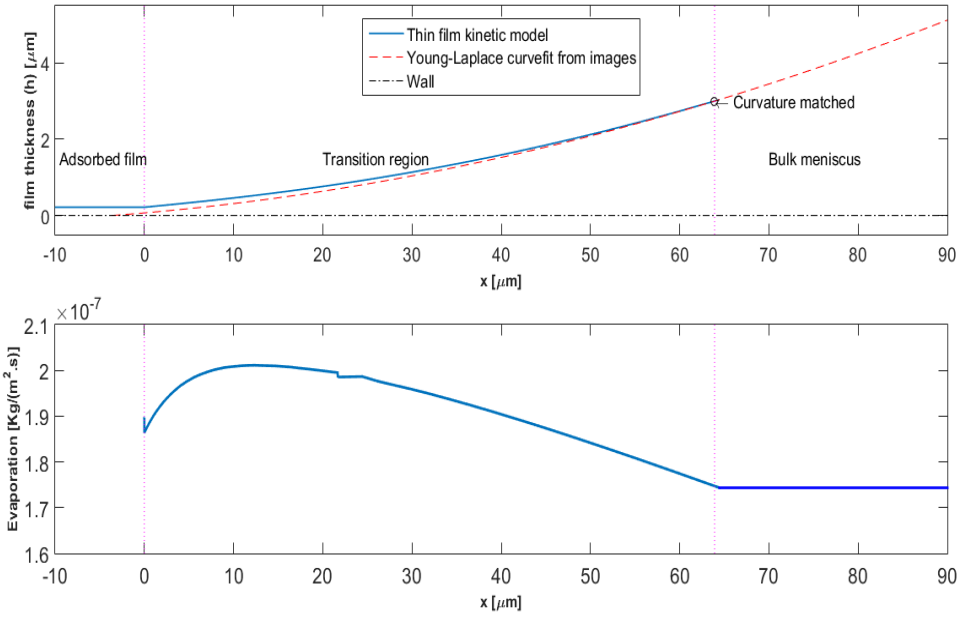

Figure 5.1: Transition film model results for saturated hydrogen at 21K, a contact angle of 0° with Al6061 using a constant wall temperature of 21.00005. The temperature of the wall, liquid and vapor is assumed to be 21K in the adsorbed film.

Chapter 6

Future Work

In addition to fulfilling the requirements for the Degree of Master of Science, this document also serves as a proposal for the PhD program. This section details the proposed study along with the approach to reach the set objectives. The objectives of the research effort are listed below:

1. To calculate accommodation coefficients for hydrogen and methane considering the physics of the contact line region

2. To determine whether the accommodation coefficient is a thermodynamic property of the fluid

Historically measured coefficients made use of a planar bulk model and it has been shown that this approach is incorrect. The first objective of the proposed work aims at addressing one of the possible reasons why the previously measured values of accommodation coefficients are inconsistent. The proposed method takes into account the interface curvature, disjoining pressure and thin film fluid physics such as the non-uniform evaporation that occurs in the contact line region. The effect of the variable temperature of solid phase in the vicinity of the contact line is also included. Further, the collisional effects in the knudsen layer of the interface resulting in a non-Maxwellian velocity distribution is incorporated. The accommodation coefficients for hydrogen and methane will be determined using a combination of neutron imaging cryo experiments, CFD thermal model and the transition film kinetic model for different test conditions.

The second objective is met by analyzing the variability of the extracted accommodation coefficients to temperature/pressure, contact line length and the solid phase. The results of the sensitivity will shed light on whether the accommodation coefficient is truly a thermodynamic property. If the extracted coefficients do not vary with contact line length or the solid phase, it can be safely assumed that the accommodation coefficient is indeed a thermodynamic property of the fluid. However, if the extracted coefficients vary arbitrarily despite a systematic analysis, kinetic theory may be an inappropriate approach to model meniscus phase change.

Listed below is the approach and specific tasks to reach the specified objectives. Figure 6.1 shows the proposed timeline for the study.

1. **Cryogenic neutron imaging phase change tests at NIST**

   The following experiments have already been successfully carried out at NIST for pure methane and hydrogen and will be used to extract accommodation coefficients

   (a) Tests with liquid hydrogen and liquid methane at different saturation pressures varying between 15 psia and 30 psia

   (b) Phase change tests with SS and Al testcells of different diameters to vary the surface energy and contact line length, respectively.

   (c) Image processing and data analysis to determine phase change rates.

   (d) Determine meniscus curvature to establish physical boundary conditions for the transition film model

2. **CFD thermal modeling of heat transfer in the cryostat**

   (a) Dry test modeling of the sample well to match the transient heat transfer characteristics of the cryostat

   (b) A line sink simulation to extract interior wall temperatures

3. **Molecular dynamics**

(a) Extract velocity distribution to modify evaporation model

(b) Determine adsorbed film thickness to establish initial condition for the transition film model

4. **Kinetic modeling of the meniscus phase change**

(a) Build basic model using the Hertz-Knudsen-Schrage equation

(b) Implement a variable wall temperature feature

(c) Reformulate model using velocity distribution from MD simulations

(d) Determine accommodation coefficients for hydrogen and methane for different contact line lengths and solid phases

(e) Sensitivity analysis

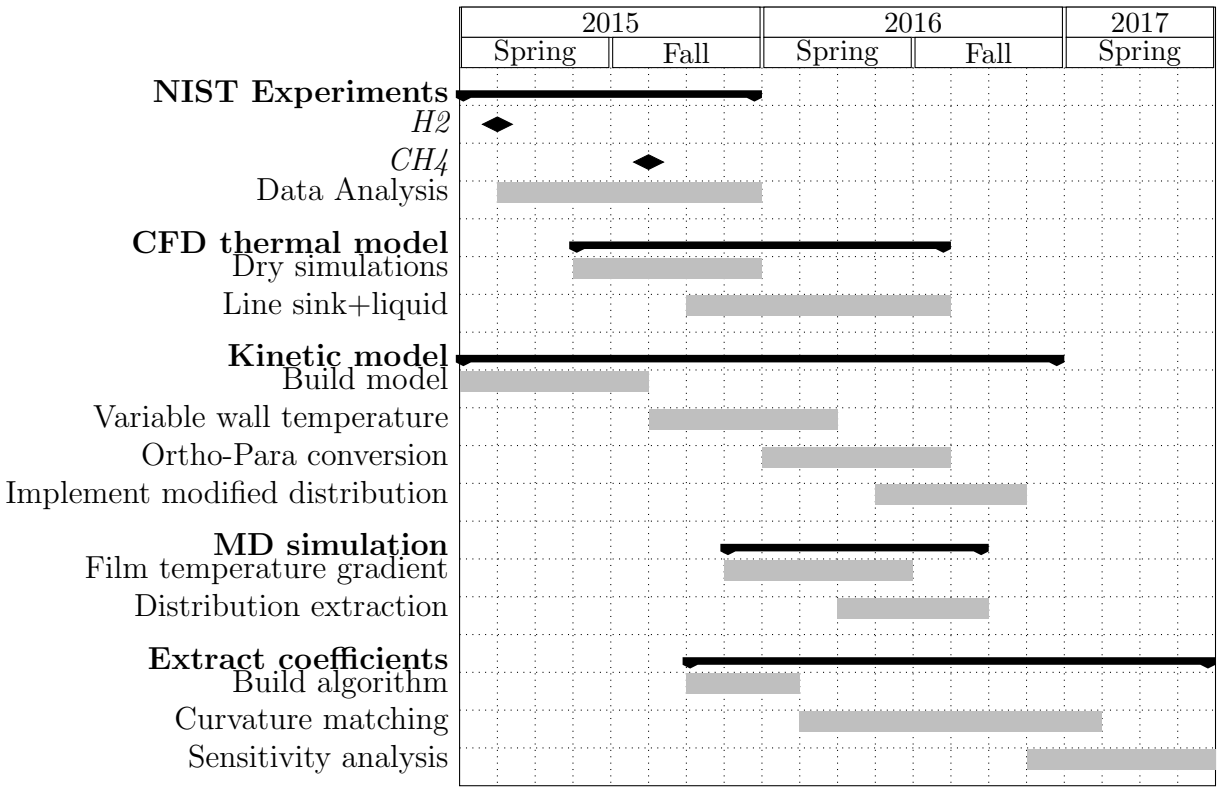

Figure 6.1: Proposed timeline

References

[1] K. Bellur, E. F. Medici, M. Kulshreshtha, V. Konduru, D. Tyrewala, A. Tamilarasan, J. McQuillen, L. Juscelino, D. Hussey, D. Jacobson, J. Scherschligt, J. Hermanson, C. K. Choi, and J. S. Allen, "A new experiment for investigating evaporation and condensation of cryogenic propellants," *Cryogenics*, 2015.

[2] N. R. Council, *NASA Space Technology Roadmaps and Priorities: Restoring NASA's Technological Edge and Paving the Way for a New Era in Space"*. Washington, DC: The National Academies Press, 2012.

[3] J. Hartwig and J. McQuillen, "Analysis of screen channel lad bubble point tests in liquid oxygen at elevated temperature," in *42nd AIAA Thermophysics Conference, Honolulu, HI*, 2011.

[4] J. Hartwig and J. McQuillen, "Analysis of screen channel lad bubble point tests in liquid methane at elevated temperature," in *50st Aerospace Sciences Meeting, Nashville, TN*, 2012.

[5] J. Hartwig, J. McQuillen, and D. Chato, "Performance gains of propellant management devices for liquid hydrogen depots," in *51st Aerospace Sciences Meeting, Grapevine, TX*, 2013.

[6] C. Panzarella and M. Kassemi, "On the validity of purely thermodynamic descriptions of two-phase cryogenic fluid storage," *Journal of Fluid Mechanics*, vol. 484, pp. 41–68, 6 2003.

[7] C. Panzarella, D. Plachta, and M. Kassemi, "Pressure control of large cryogenic tanks in microgravity," *Cryogenics*, vol. 44, no. 6, pp. 475–483, 2004.

[8] C. Panzarella and M. Kassemi, "Self-pressurization of large spherical cryogenic tanks in space," *Journal of spacecraft and rockets*, vol. 42, no. 2, pp. 299–308, 2005.

[9] S. Barsi, M. Kassemi, C. Panzarella, and J. I. D. Alexander, "A tank self-pressurization experiment using a model fluid in normal gravity," *AIAA-2005-1143, January*, 2005.

[10] C. Panzarella and M. Kassemi, "One-dimensional model of evaporation and condensation in the presence of a noncondensable gas with applications to cryogenic fluid storage," *International Journal of Heat and Mass Transfer*, vol. 52, no. 15, pp. 3767–3777, 2009.

[11] V. Ajaev, *Interfacial fluid mechanics*. Springer, 2012.

[12] J. L. Plawsky, M. Ojha, A. Chatterjee, and P. Wayner, "Review of the effects of surface topography, surface chemistry, and fluid physics on evaporation at the contact line," *Chemical Engineering Communications*, vol. 196, no. 5, pp. 658–696, 2008.

[13] G. Preiss and P. Wayner, "Evaporation from a capillary tube," *Journal of Heat Transfer*, vol. 98, no. 2, pp. 178–181, 1976.

[14] P. Wayner, "The effect of interfacial mass transport on flow in thin liquid films," *Colloids and Surfaces*, vol. 52, pp. 71–84, 1991.

[15] R. Marek and J. Straub, "Analysis of the evaporation coefficient and the condensation coefficient of water," *International Journal of Heat and Mass Transfer*, vol. 44, no. 1, pp. 39–53, 2001.

[16] H. Cammenga, H. Klinge, and B.-E. Rudolph, "Untersuchungen ber die verdampfungs-geschwindigkeit von flssigkeiten," *Fortschrittsberichte ber Kolloide und Polymere*, vol. 55, no. 1, pp. 118–123, 1971.

[17] D. L. Fritz III, *Implementation of a phenomenological evaporation model into a porous network simulation for water management in low temperature fuel cells.* PhD thesis, Michigan Technological University, 2012.

[18] S. S. Panchamgam, A. Chatterjee, J. L. Plawsky, and P. Wayner, "Comprehensive experimental and theoretical study of fluid flow and heat transfer in a

microscopic evaporating meniscus in a miniature heat exchanger," *International Journal of Heat and Mass Transfer*, vol. 51, no. 21, pp. 5368–5379, 2008.

[19] H. Hertz, "Ueber die verdunstung der flüssigkeiten, insbesondere des quecksilbers, im luftleeren raume," *Annalen der Physik*, vol. 253, no. 10, pp. 177–193, 1882.

[20] M. Knudsen, "Maximum rate of vaporization of mercury," *Ann. Phys*, vol. 47, pp. 697–705, 1915.

[21] R. W. Schrage, *A theoretical study of interphase mass transfer*. Columbia University Press, 1953.

[22] J. Barrett and C. Clement, "Kinetic evaporation and condensation rates and their coefficients," *Journal of colloid and interface science*, vol. 150, no. 2, pp. 352–364, 1992.

[23] S.-K. Wee, K. D. Kihm, D. M. Pratt, and J. S. Allen, "Microscale heat and mass transport of evaporating thin film of binary mixture," *Journal of thermophysics and heat transfer*, vol. 20, no. 2, pp. 320–326, 2006.

[24] P. von der Hardt and H. Röttger, *Neutron radiography handbook: nuclear science and technology*. Springer Science & Business Media, 2012.

[25] K. Hartmut and K. Ernst, "Photographic detection of slowly moving neutrons," Jan. 9 1940. US Patent 2,186,757.

[26] S. Körner, "Digital image processing in neutron radiography," 2000.

[27] K. Mishima and T. Hibiki, "Development of high-frame-rate neutron radiography and quantitative measurement method for multiphase flow research," *Nuclear Engineering and Design*, vol. 184, no. 2, pp. 183–201, 1998.

[28] M. Strobl, I. Manke, N. Kardjilov, A. Hilger, M. Dawson, and J. Banhart, "Advances in neutron radiography and tomography," *Journal of Physics D: Applied Physics*, vol. 42, no. 24, p. 243001, 2009.

[29] B. Derjaguin and Z. Zorin, "Optical study of the adsorption and surface condensation of vapours in the vicinity of saturation on a smooth surface," *Progress in Surface Science*, vol. 40, no. 1, pp. 83–117, 1992.

[30] F. Holm and S. Goplen, "Heat transfer in the meniscus thin-film transition region," *Journal of Heat Transfer*, vol. 101, no. 3, pp. 543–547, 1979.

[31] Q. Wu and H. Wong, "A slope-dependent disjoining pressure for non-zero contact angles," *Journal of Fluid Mechanics*, vol. 506, pp. 157–185, 2004.

[32] A. Lotfi, J. Vrabec, and J. Fischer, "Evaporation from a free liquid surface," *International Journal of Heat and Mass Transfer*, vol. 73, pp. 303–317, 2014.

[33] G. A. Bird, "Molecular gas dynamics and the direct simulation of gas flows," 1994.

[34] P. L. Bhatnagar, E. P. Gross, and M. Krook, "A model for collision processes in gases. i. small amplitude processes in charged and neutral one-component systems," *Physical review*, vol. 94, no. 3, p. 511, 1954.

[35] P. Welander, "On the temperature jump in a rarefied gas," *Arkiv fysik*, vol. 7, 1954.

[36] T. Ytrehus, "Theory and experiments on gas kinetics in evaporation," *Rarefied Gas Dynamics*, vol. 2, pp. 1197–1212, 1977.

[37] D. Labuntsov and A. Kryukov, "Analysis of intensive evaporation and condensation," *International Journal of Heat and Mass Transfer*, vol. 22, no. 7, pp. 989–1002, 1979.

[38] J. Yu and H. Wang, "A molecular dynamics investigation on evaporation of thin liquid films," *International Journal of Heat and Mass Transfer*, vol. 55, no. 4, pp. 1218–1225, 2012.

[39] C. Ji and Y. Yan, "A molecular dynamics simulation of liquid–vapour–solid system near triple-phase contact line of flow boiling in a microchannel," *Applied thermal engineering*, vol. 28, no. 2, pp. 195–202, 2008.

[40] S. Maroo and J. Chung, "Molecular dynamic simulation of platinum heater and associated nano-scale liquid argon film evaporation and colloidal adsorption characteristics," *Journal of colloid and interface science*, vol. 328, no. 1, pp. 134–146, 2008.

[41] T. Tsuruta, H. Tanaka, and T. Masuoka, "Condensation/evaporation coefficient and velocity distributions at liquid–vapor interface," *International Journal of Heat and Mass Transfer*, vol. 42, no. 22, pp. 4107–4116, 1999.

[42] M. Bond and H. Struchtrup, "Mean evaporation and condensation coefficients based on energy dependent condensation probability," *Physical Review E*, vol. 70, no. 6, p. 061605, 2004.

[43] P. Rahimi and C. Ward, "Kinetics of evaporation: statistical rate theory approach," *Int. J. of Thermodynamics*, vol. 8, no. 1, p. 1, 2005.

[44] C. Ward and D. Stanga, "Interfacial conditions during evaporation or condensation of water," *Physical Review E*, vol. 64, no. 5, p. 051509, 2001.

[45] G. Fang and C. Ward, "Temperature measured close to the interface of an evaporating liquid," *Physical Review E*, vol. 59, no. 1, p. 417, 1999.

[46] C. Cercignani, *Rarefied gas dynamics: from basic concepts to actual calculations*, vol. 21. Cambridge University Press, 2000.

[47] S. Chapman and T. G. Cowling, *The mathematical theory of non-uniform gases: an account of the kinetic theory of viscosity, thermal conduction and diffusion in gases*. Cambridge university press, 1970.

[48] G. Nagayama and T. Tsuruta, "A general expression for the condensation coefficient based on transition state theory and molecular dynamics simulation," *The Journal of chemical physics*, vol. 118, no. 3, pp. 1392–1399, 2003.

[49] C. Ward and G. Fang, "Expression for predicting liquid evaporation flux: Statistical rate theory approach," *Physical Review E*, vol. 59, no. 1, p. 429, 1999.

[50] G. Fang and C. Ward, "Examination of the statistical rate theory expression for liquid evaporation rates," *Physical Review E*, vol. 59, no. 1, p. 441, 1999.

[51] J. Fischer, "Distribution of pure vapor between two parallel plates under the influence of strong evaporation and condensation," *Physics of Fluids (1958-1988)*, vol. 19, no. 9, pp. 1305–1311, 1976.

[52] M. Matsumoto, "Molecular dynamics of fluid phase change," *Fluid phase equilibria*, vol. 144, no. 1, pp. 307–314, 1998.

[53] J. N. Israelachvili, *Intermolecular and surface forces: revised third edition*. Academic press, 2011.